

A fermion-parity qubit in a proximitized double quantum dot

Max Geier,¹ Rubén Seoane Souto,^{1,2,3,4} Jens Schulenburg,^{1,5}
Serwan Asaad,¹ Martin Leijnse,^{1,2} and Karsten Flensberg^{1,6}

¹*Center for Quantum Devices, Niels Bohr Institute,
University of Copenhagen, 2100 Copenhagen, Denmark*

²*Division of Solid State Physics and NanoLund, Lund University, 22100 Lund, Sweden*

³*Departamento de Física Teórica de la Materia Condensada,
Condensed Matter Physics Center (IFIMAC) and Instituto Nicolás Cabrera,
Universidad Autónoma de Madrid, 28049 Madrid, Spain*

⁴*Instituto de Ciencia de Materiales de Madrid (ICMM),
Consejo Superior de Investigaciones Científicas (CSIC),
Sor Juana Inés de la Cruz 3, 28049 Madrid, Spain.*

⁵*Department of Microtechnology and Nanoscience (MC2),
Chalmers University of Technology, S-412 96 Göteborg, Sweden*

⁶*NNF Quantum Computing Programme, Niels Bohr Institute,
University of Copenhagen, 2100 Copenhagen, Denmark*

(Dated: July 13, 2023)

Bound states in quantum dots coupled to superconductors can be in a coherent superposition of states with different electron number but with the same number parity. Electrostatic gating can tune this superposition to a sweet spot, where the quantum dot has the same mean electric charge independent of its electron-number parity. Here, we propose to encode quantum information in the local fermion parity of two tunnel-coupled quantum dots embedded in a Josephson junction. At the sweet spot, the qubit states have zero charge dipole moment. This protects the qubit from dephasing due to electric field fluctuations. Depending on the strength of the tunnel coupling between the dots, the system is further protected towards either relaxation (weak tunneling) or dephasing (strong tunneling) from noise coupling separately to each quantum dot. We describe initialization and readout as well as single-qubit and two-qubit gates by pulsing gate voltages.

I. INTRODUCTION

Quantum dots coupled to superconductors host bound states with energies below the superconducting gap. They are known as Yu-Shiba-Rusinov states [1–3] for large charging energy or Andreev bound states [4] with small charging energy compared to the superconducting gap. These bound states are superpositions with different particle number due to so-called Andreev tunnel events where pairs of electrons in the quantum dot are transferred as a Cooper pair in the superconductor. This process thus preserves the total fermion parity of the system. In recent years, hybrid superconductor-semiconductor structures have proven to be a reliable platform to realize Josephson junctions, qubits, and quantum dot systems whose properties depend on the occupation of the in-gap bound states. These systems have been extensively studied experimentally [5–29], and theoretically [30–44].

Electrostatic gating can control the mean electric charge of the subgap states [17–19, 43–46]. The quantum dot can be tuned to a “sweet spot” where it has same mean electric charge for both ground states with an even or odd electron number parity. As a consequence, both fermion parity sectors have the same response to small electric fields.

Here, we propose to leverage the protection of the local fermion parity together with the tunability of the charge expectation value to define a qubit in a pair of electrostatically controlled quantum dots embedded in a super-

conducting loop, see sketch in Fig. 1(a). The two qubit states are encoded in the local fermion parity of the two dots: the state $|L\rangle$ ($|R\rangle$) is a product of the left (right) quantum dot hosting an odd number of fermions while the right (left) quantum dot hosts an even number, as depicted in Fig. 1(b). Both quantum dots are tuned to the sweet spot where even and odd fermion parity sectors have the same mean electric charge, causing insensitivity to small fluctuations of the electrostatic environment. The quantum dot with odd fermion parity has a spin $1/2$ degree of freedom. When the coupling of the spin to the environment is negligible, the qubit can be operated with spin-degenerate levels. Otherwise, the spin can be polarized by an applied magnetic field.

The coherence properties of this system depends on the hybridization between the quantum dots. For weak hybridization, the qubit eigenstates are localized in $|L\rangle$ and $|R\rangle$. Depolarization of the qubit state requires a quasiparticle to tunnel between the quantum dots, which is suppressed for weak tunneling. In this regime, dephasing due to noise coupling to individual quantum dots (such as local magnetic field or level energy fluctuations) are further suppressed. Instead, the qubit is sensitive to fluctuations in the tunneling strength.

When charging energy can be neglected, the qubit states can be described in terms of a single Bogoliubov quasiparticle shared between the quantum dots. This quasiparticle has zero electric charge when the quantum dots are tuned to the sweet spot. From this point of view, our proposal can be considered a “chargeless” variant of a

charge qubit [47, 48], where the electron position encodes quantum information. In our parity qubit, the superconducting correlations strip of the electron's charge.

In the following Sec. II, we define the system Hamiltonian and the regimes for qubit operations, as well as microwave controlled single- and two-qubit rotations. A detailed discussion on the effects of noise on the qubit is contained in Sec. III. In Sec. IV, we discuss the relation of our proposal to other qubit realizations. We comment on the feasibility of our proposal in currently available material platforms in Sec. V.

II. THE FERMION-PARITY QUBIT

In this section, we define the Hamiltonian describing the pair of quantum dots connected to superconductors (Sec. II A), identify the operating regimes (Sec. II B), and describe initialization and read-out (Sec. II C) as well as single- and two-qubit rotations (Sec. II D and II E).

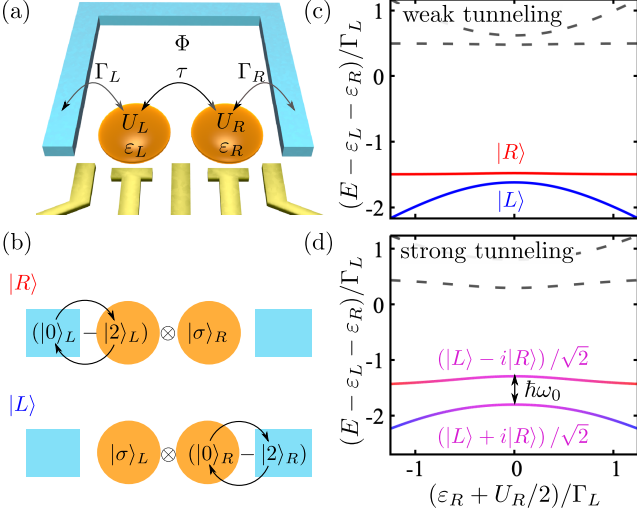


Figure 1. (a) Device sketch: Two quantum dots labeled by $\nu = L, R$ (orange) with charging energy U_ν are coupled to a superconducting loop (light blue) inducing superconducting correlations with magnitude Γ_ν and phase difference $\phi = 2\pi\Phi/\Phi_0$ controlled by the enclosed magnetic flux Φ , where $\Phi_0 = h/2e$ is the superconducting flux quantum. The dot level energies ε_ν and interdot coupling τ are tunable by gate electrodes (yellow). (b) Sketch of the qubit states $|L\rangle$ and $|R\rangle$, which are a product of single electrons of spin σ , $|\sigma\rangle_\nu = \hat{c}_{\nu\sigma}^\dagger|0\rangle_\nu$, and even parity states in an equal superposition of empty $|0\rangle_\nu$ and double occupation $|2\rangle_\nu = \hat{c}_{\nu\uparrow}^\dagger\hat{c}_{\nu\downarrow}^\dagger|0\rangle_\nu$. (c) Many-body spectrum as a function of level energy $\varepsilon_R + U_R/2$ for weak tunneling. The blue (red) solid line indicates the qubit state $|L\rangle$ ($|R\rangle$), while dashed lines are excited states. Parameters: $\tau = \Gamma_L/20$, $\Gamma_R = 1.1\Gamma_L$, $U_L = U_R = \Gamma_L$, $\varepsilon_L = -U_L/2$. (d) Corresponding results for strong tunneling. The line color indicates the wave function overlap with $|L\rangle$ (blue) and $|R\rangle$ (red). Parameters: $\tau = \Gamma_L/4$, remaining parameters unchanged.

A. System Hamiltonian

Figure 1(a) shows a sketch of the fermion-parity qubit setup with the relevant control parameters. The system Hamiltonian,

$$\hat{H} = \sum_\nu \hat{H}_\nu + \hat{H}_T, \quad (1)$$

is composed of terms \hat{H}_ν , $\nu = L, R$ describing the two individual quantum dots and their tunnel coupling \hat{H}_T . The terms \hat{H}_ν describing the individual quantum dots read

$$\hat{H}_\nu = \sum_\sigma \varepsilon_\nu \hat{n}_{\sigma\nu} + U_\nu \hat{n}_{\uparrow\nu} \hat{n}_{\downarrow\nu} + \Gamma_\nu (\hat{c}_{\uparrow\nu} \hat{c}_{\downarrow\nu} + \text{H.c.}), \quad (2)$$

where $\hat{n}_{\sigma\nu} = \hat{c}_{\sigma\nu}^\dagger \hat{c}_{\sigma\nu}$, with the annihilation operator $\hat{c}_{\sigma\nu}$ for an electron on the dot ν with spin $\sigma = \uparrow, \downarrow$. The level energy ε_ν can be controlled using electrostatic gates, U_ν is the Coulomb repulsion strength, and Γ_ν describes the proximity-induced superconducting correlations in the quantum dots, assuming $\Delta \gg \Gamma_\nu, \varepsilon_\nu, U_\nu$ [see App. A for a discussion on the validity of the approximation]. The eigenstates of the \hat{H}_ν with even local fermion parity are superpositions of zero $|0\rangle_\nu$ and two excess electrons of opposite spin $|2\rangle_\nu = \hat{c}_{\nu\uparrow}^\dagger \hat{c}_{\nu\downarrow}^\dagger |0\rangle_\nu$. The odd local fermion parity subspace contains the states where a single electron of spin σ occupies the quantum dot, $|\sigma\rangle_\nu = \hat{c}_{\nu\sigma}^\dagger |0\rangle_\nu$. The tunnel coupling between the dots is given by

$$\hat{H}_T = \tau \sum_\sigma e^{i\phi/2} \hat{c}_{\sigma R}^\dagger \hat{c}_{\sigma L} + \text{H.c.}, \quad (3)$$

where τ is the tunneling amplitude and ϕ the superconducting phase difference. The Hamiltonian is written in a gauge where the pairing amplitudes Γ_ν are real and positive while the superconducting phase difference is included in the tunneling term. For now, spin-orbit coupling and Zeeman field are neglected as these terms are not required for operating the fermion-parity qubit. These effects are included in the discussion on dephasing and depolarization due to parameter fluctuations in Sec. III.

Single-particle picture in the absence of charging energy.— For $U_L = U_R = 0$, the system can be described in terms of Bogoliubov quasiparticles $\hat{\gamma}_{\sigma\nu}$ obtained as the eigenstates of each quantum dot Hamiltonian Eq. (2) after a Bogoliubov transformation. At the sweet spot, the Bogoliubov quasiparticles $\hat{\gamma}_{\sigma\nu} = u^* \hat{c}_{\sigma\nu} + v \hat{c}_{\sigma\nu}^\dagger$ are equal superpositions $|u|^2 = |v|^2$ of electrons and holes of opposite spin $\bar{\sigma}$ with mean electric charge $-|e|(|u|^2 - |v|^2) = 0$. The qubit basis states are constructed with the Bogoliubov quasiparticles as excitations $|\nu\rangle = \hat{\gamma}_{\sigma\nu}^\dagger |\text{BCS}\rangle$ from the ground state $|\text{BCS}\rangle = \hat{\gamma}_{\downarrow L} \hat{\gamma}_{\uparrow L} \hat{\gamma}_{\downarrow R} \hat{\gamma}_{\uparrow R} |0\rangle$. Including tunneling between the quantum dots, the eigenstates of the full Hamiltonian Eq. (1) are superpositions of $\hat{\gamma}_{\sigma L}$ and $\hat{\gamma}_{\sigma R}$. In this picture, the qubit is defined by the position of a single, chargeless Bogoliubov quasiparticle shared between the two quantum dots.

B. Sweet spot

Here, we describe the sweet spot where the qubit is optimally operated.

Level energies ε_ν .— The sweet spot, at which both fermion-parity sectors of a quantum dot have the same mean charge, is reached by setting the level energy to $\varepsilon_\nu = -U_\nu/2$. At this point, the quantum dot eigenstates with even fermion parity are symmetric ($\lambda_\nu = g$) and antisymmetric ($\lambda_\nu = u$) superpositions $|g/u\rangle_\nu = \frac{1}{\sqrt{2}}(|0\rangle_\nu \pm |2\rangle_\nu)$ with energies $\pm U_\nu$. Thus the ground state of individual quantum dots is $|u\rangle_\nu$.

Superconducting phase difference ϕ .— The phase difference ϕ determines the tunneling between the quantum dots. At $\phi = 0$, tunneling of an electron switches the symmetry of the even-parity bound state, due to a fermion sign acquired during tunneling. At $\phi = \pi$, this sign is cancelled and the symmetry of the even-parity bound state is preserved, thus coupling the two qubit states, which have $\lambda_R = \lambda_L = u$. We set $\phi = \pi$ such that tunneling acts within the qubit subspace. Furthermore, at $\phi = \pi$, the spectrum is first-order insensitive to the fluctuations in ϕ (see Eq. (13)).

Tunneling strength τ .— Tunneling between the quantum dots hybridizes the bound states in the two dots. Without tunnel coupling, the qubit eigenstates are the product states $|L\rangle = |\sigma\rangle_L \otimes |u\rangle_R$, $|R\rangle = |u\rangle_L \otimes |\sigma\rangle_R$ with energies $-U_{L/R}/2 - \Gamma_{R/L}$ (at the sweet spots). With finite tunneling strength and $\phi = \pi$, the qubit eigenstates are $|-\rangle = \sin \frac{\eta}{2} |L\rangle + i \cos \frac{\eta}{2} |R\rangle$, $|+\rangle = \cos \frac{\eta}{2} |L\rangle - i \sin \frac{\eta}{2} |R\rangle$ with angle

$$\tan \eta = \frac{2\tau}{(U_R - U_L)/2 - (\Gamma_R - \Gamma_L)}, \quad (4)$$

and energies $E_\rho = -(U_R + U_L)/4 - (\Gamma_R + \Gamma_L)/2 + \rho \frac{\tau}{\sin \eta}$, where $\rho = \pm$ labels the qubit states $|\pm\rangle$.

To summarize this section, setting both quantum dots to the sweet spot leads to a first-order insensitivity of the qubit frequency to the dot potentials. Qubit operation is optimal at phase bias $\phi = \pi$. Depending on whether the qubit coherence is limited by relaxation or dephasing due to noise coupling, the system can be operated in two regimes set by the tunneling strength. For weak tunneling ($|\eta| \ll 1$) the system is protected towards relaxation, but sensitive to dephasing from fluctuations of the energy difference the even and odd states of the individual dots. In contrast, for strong tunneling ($|\eta| \simeq \pi/2$) the sensitivity to these fluctuations is suppressed by a factor $|\tan \eta| \gg 1$ (but the qubit is no longer protected against relaxation). Analytic results for the decoherence rates are presented in Sec. III.

The protection from dephasing follows from the dispersion of the qubit spectrum [49]. Figure 1(c) and (d) show the many-body spectra as a function of the level energy ε_R for the two regimes. Analogous results hold for ε_L . For weak tunneling ($|\eta| \ll 1$, Figure 1(c)) the slope of the energy of the two states $|L\rangle$ and $|R\rangle$ as a function of ε_R

aligns at the sweet spot $\varepsilon_R = -U_R/2$. At this point, the qubit frequency ($\hbar\omega_0$, given by the energy difference of the two lowest states) is insensitive to first order in ε_R . For strong tunneling ($|\eta| \simeq \pi/2$, Figure 1(d)) the fluctuations of qubit frequency are further suppressed by a factor $|(U_R - U_L)/2 - (\Gamma_R - \Gamma_L)|/\tau$.

C. Initialization and read-out

The operation of our qubit proposal is restricted to total odd fermion parity in the two quantum dots. Changing the total parity in the pair of quantum dots requires a quasiparticle from the superconducting leads to enter the quantum dots, similar to a quasiparticle poisoning event [50]. It can be expected that there are (almost) no quasiparticles present in the superconducting leads for temperature much below their superconducting gap. However, recent experiments [51–55] have shown that superconductors exhibit a density of “hot” quasiparticles at high energy that persists for small temperatures and dominates over thermally excited quasiparticles below $T \approx 35\text{mK}$ [53] or $T \approx 150\text{mK}$ [51, 52, 54]. Below, we discuss two ways to control fermion-parity changing events to initialize the fermion parity of the individual quantum dots.

Initialization by detuning ε_ν .— Depending on the system parameters, it may be energetically favorable for a quasiparticle from the environment to enter a quantum dot and, thereby, flip its fermion parity. For large charging energy $U > \Gamma_\nu$, the ground state of the quantum dot switches from odd fermion parity around the sweet spot (in our model: $(\varepsilon_\nu - U_\nu/2)^2 \leq \Gamma_\nu^2$) to even at larger level energy ε_ν [17, 43, 44, 56]. The energy released by a quasiparticle entering the quantum dot depends on the parity of the quantum dot, resulting in different quasiparticle trapping rates [57]. This transition has been applied experimentally to initialize the fermion parity in a quantum dot [58]. A follow-up work, Ref. 21, applied this procedure to initialize a quantum dot in the odd-parity sector, with measured even-to-odd and odd-to-even switching rates of 17 kHz and 0.36 kHz, respectively. If the fermion parity lifetimes cannot be tuned to differ significantly, one can alternatively monitor the fermion parity on the quantum dots in real time.

Initialization by microwave drive.— Alternatively, the local fermion parity can be polarized in the odd parity state by a microwave pulse on a local gate that supplies the energy to split a Cooper pair from the condensate into one electron in the dot and one in the continuum of the superconductor [59]. Similarly, the local fermion parity can be polarized in the even state by a microwave pulse that supplies the energy to excite an electron from the dot into the continuum of the superconductor.

Comment on spin initialization.— In the absence of Zeeman fields, the above initialization procedures do not favor a particular spin direction in the quantum dot. In this case, the spin of the quasiparticle is irrelevant and

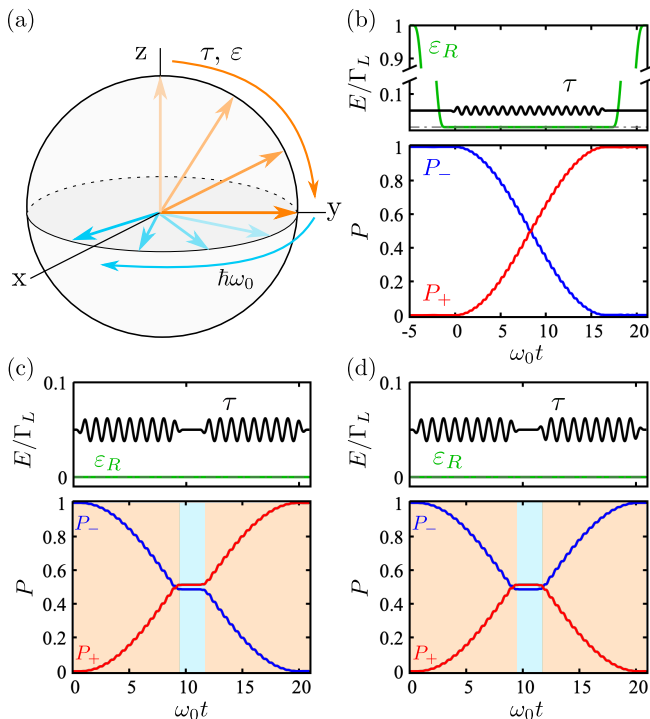


Figure 2. Two axis control of the parity qubit operated at weak tunneling $|\eta| \ll 1$. (a) Sketch of the rotations. A drive of the tunneling τ or detuning ε_ν performs X or Y rotations. The energy difference between the two qubit states leads to a natural rotation around Z with the qubit frequency ω_0 . (b) Pauli X -gate by driving the tunnel coupling τ at the sweet spot. The probabilities $P_{\pm}(t) = |\langle \pm | \Psi(t) \rangle|^2$ describe the overlap of the driven wavefunction $|\Psi(t)\rangle$ with the qubit eigenstates $|-\rangle \approx |L\rangle$ and $|+\rangle \approx |R\rangle$ (for weak tunneling). (c) $X_{\pi/2}Z_{2n\pi}X_{\pi/2} = X_\pi$ sequence of rotations, the waiting time is chosen as $t_w = n/\omega_0$, $n = 1, 2, 3, \dots$ such that $Z_{2n\pi} = \mathbf{1}$. (d) Shifting the phase of the second pulse by $\phi_0 = \pi$ rotates the qubit back to its initial configuration, $X_{\pi/2}Z_{2n\pi}X_{-\pi/2} = \mathbf{1}$. In (b) to (d), we include a ramp in ε_R at the beginning and end of the qubit operation, which simulates detuning the quantum dot away from the sweet spot for initialization and read-out. Hamiltonian parameters are the same as in Fig. 1(c). The qubit frequency at the sweet spot is $\hbar\omega_0 \approx 0.1414 \Gamma_L$. The parameterization of the pulses is contained in App. D.

plays no role during operations.

Read-out by charge measurements.— The qubit state can be read out by a converting the parity information to charge. This is done by detuning the level energy of one of the quantum dots away from the sweet spot (to $|\varepsilon_\nu + U_\nu/2| \gtrsim \Gamma_\nu$), resulting in a different charge in the dots for the even and odd parity sectors. Once tuned away, the state can be read by conventional charge-detection methods [60–63].

D. Single-qubit gates

Single-qubit gates can be achieved by driving either the tunneling amplitude between the dots $\tau(t) = \tau + \delta\tau \cos(\Omega t + \varphi_0)$ or the level energy of one of the quantum dots $\varepsilon_\nu(t) = \varepsilon_\nu + \delta\varepsilon_\nu \cos(\Omega t + \varphi_0)$ at the resonance frequency $\Omega = \omega_0 = (E_+ - E_-)/\hbar$ [Fig. 2(a)]. The two computational qubit eigenstates $|-\rangle$ and $|+\rangle$ are given by the two lowest-energy eigenstates in the global odd-parity sector of $\hat{H}(t)$ [defined around Eq. (4)]. The amplitudes $\delta\tau, \delta\varepsilon$ determine the Rabi frequency, and the phase φ_0 sets the axis of rotation within the X - Y -plane [64]. We obtain the response of the qubit states to the driving protocol from the exact unitary Schrödinger evolution with respect to $\hat{H}(t)$ [Eq. (1)].

Weak tunneling regime, $|\eta| \ll 1$.— In the weak tunneling regime, the qubit eigenbasis $|\pm\rangle$ is approximately given by the product states $|-\rangle \approx |L\rangle$ and $|+\rangle \approx |R\rangle$, up to perturbative corrections in $|\tan \eta| \ll 1$. In this basis, the tunnel coupling \hat{H}_T at $\phi = \pi$ is off-diagonal, $\hat{H}_T|L\rangle = |R\rangle$. Thus, a drive in the tunnel strength leads to qubit rotations.

The qubit rotation by driving τ is demonstrated in Fig. 2(b). There, we furthermore include a ramp of the level energy ε_R at the beginning and end of the protocol to demonstrate a read-out scenario where adiabatic detuning of ε_R changes the mean charge of the even-parity state detectable by a charge measurement. The small modulation on top of the Rabi oscillations is due to the Bloch-Siegert effect [65] occurring for sizable ratios $\delta\tau/\Omega$ between Rabi and driving frequency. These oscillations are often neglected when employing a rotating-wave approximation for driven quantum systems, but are included in our exact time-evolution.

Due to the finite energy difference between the two qubit states, any superposition between the qubit states Larmor precesses at frequency ω_0 around the Z -axis [Fig. 2(a)]. Changing the phase ϕ_0 of the pulse relative to the Larmor precession of the qubit changes the axis of rotation. This is demonstrated in Figs. 2(c,d): In Fig. 2(c), two $X_{\pi/2}$ pulses are applied in sequence separated by a waiting time t_w . The waiting time is chosen as $\omega_0 t_w = 2\pi n$ such that the rotation $Z_{\omega_0 t_w} = \mathbf{1}$. The result is $X_{\pi/2}Z_{\omega_0 t_w}X_{\pi/2} = X_\pi$. In Fig. 2(d), the phase of the second pulse is shifted by $\phi_0 = \pi$ such that its rotation in the opposite direction $X_{-\pi/2}$ brings the qubit back into its initial state.

Strong tunneling regime, $|\eta| \approx \pi/2$.— For strong tunneling, the eigenstates $|\pm\rangle$ are approximately equal superpositions of the product states $|L\rangle$ and $|R\rangle$, up to perturbative corrections in $\cot \eta$. In this case, driving the amplitude τ only affects weakly the qubit states via perturbative processes in $\cot \eta$. Instead, driving the level energy ε_ν of one of the quantum dots strongly couples to the qubit states. A numerical demonstration of the resulting Rabi oscillations is shown in Fig. 3. Away from the sweet spot, the optimal driving frequency for Rabi processes equals to the qubit frequency. At the sweet

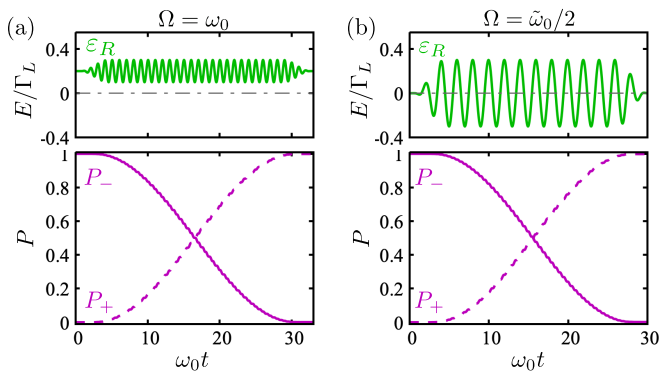


Figure 3. Pauli X gate for strong tunnel coupling $|\eta| \approx \pi/2$, implemented by (a) driving ε_R away from the sweet spot $\varepsilon_R = -U_R/2 + \delta\varepsilon_{R,\text{detune}}$ in resonance $\Omega = \omega_0(-U_R/2 + \delta\varepsilon_{R,\text{detune}})$, or by (b) driving ε_R at half of the qubit frequency averaged over one period of the drive, $\Omega = \frac{\bar{\omega}}{2} = \frac{1}{2}(\omega_0 + \frac{1}{8} \frac{\partial^2 \omega_0}{\partial \varepsilon_\nu^2} \delta \varepsilon_\nu^2)$. Hamiltonian parameters are the same as in Fig. 1(d). The qubit frequency at the sweet spot is $\hbar\omega_0 \approx 0.5099 \Gamma_L$. The parameterization of the pulses is contained in App. D. With our parameters, the ground state is $|+\rangle$ as $\eta < 0$.

spot, the optimal driving frequency to achieve complete population transfer is shifted to $\Omega = \frac{1}{2}(\omega_0 + \frac{1}{8} \frac{\partial^2 \omega_0}{\partial \varepsilon_\nu^2} \delta \varepsilon_\nu^2)$. The second term in the previous expression accounts for the shift of the mean qubit frequency at the sweet spot in the presence of the drive with amplitude $\delta\varepsilon_\nu$ in second-order perturbation theory, see App. B for a derivation. The derivative of the qubit frequency $\frac{\partial^2 \omega_0}{\partial \varepsilon_\nu^2}$ follows directly from the perturbative result contained in Eq. (12) below. Again, two-axis control is achieved by setting the phase ϕ_0 of the pulse or, equivalently, by Larmor precession due to the energy difference of the two qubit states.

E. Two-qubit gates

We describe two-qubit gates that arise from inductive coupling of the superconducting loops or capacitive coupling between quantum dots of two distinct qubits indexed by $j = 1, 2$. Figure 4 shows a sketch for a setup allowing to realize two-qubit gates.

Capacitive coupling.— Mutual capacitive coupling between quantum dots ν_1, ν_2 of adjacent qubits can be described by an interaction term $U_{12} \hat{n}_{\nu_1,1} \hat{n}_{\nu_2,2}$, where $\hat{n}_{\nu_j,j} = \sum_\sigma \hat{n}_{\sigma,\nu_j,j}$ is the occupation of the $\nu_j = L, R$ quantum dot of qubit $j = 1, 2$. For concreteness, we consider capacitive coupling between the right quantum dot $\nu_{R,1}$ of qubit 1 and the left quantum dot $\nu_{L,2}$ of qubit 2. Using $\hat{n}_{\nu,j} = \frac{d\hat{H}_j}{d\varepsilon_{\nu,j}}$ with \hat{H}_j being the Hamiltonian Eq. (1) for each qubit, we apply the Hellman-Feynman theorem $\langle n | \frac{d\hat{H}}{d\varepsilon_{\nu,j}} | n \rangle = \frac{dE_n}{d\varepsilon_{\nu,j}}$ where $|n\rangle$ labels the n 'th eigenstate. The capacitive coupling projected onto the

qubit eigenspace is

$$\mathcal{P} U_{12} \hat{n}_{R1} \hat{n}_{L2} \mathcal{P} = \hbar^2 U_{12} \frac{d\omega_{0,1}}{d\varepsilon_{R,1}} \frac{d\omega_{0,2}}{d\varepsilon_{L,2}} \hat{\rho}_1^z \otimes \hat{\rho}_2^z, \quad (5)$$

where $\hat{\rho}_j^z$ are Pauli- z operators in the space of eigenstates $|\rho_j\rangle_j$, $\rho_j = \pm$ of qubit j (see around Eq. (4) for a definition of the qubit eigenstates at the operating point), $\mathcal{P} = \sum_{\rho_1, \rho_2} |\rho_1\rangle_1 |\rho_2\rangle_2 \langle \rho_1|_1 \langle \rho_2|_2$ the projector onto these states, and the qubit frequency $\hbar\omega_{0,j}$ to second order is given in Eq. (12) below. At the sweet spot, $\varepsilon_{\nu,j} = -U_{\nu,j}/2$, the capacitive coupling does not differentiate between the qubit states as the charge dipole moment of both qubit states vanishes. The charge dipole moment increases linearly with the detuning of the level energy $\varepsilon_{\nu,j}$ away from the sweet spot, which allows to switch on the two-qubit coupling using electrostatic control of the level energy $\varepsilon_{\nu,j}$. [66] Long distance capacitive coupling between quantum dots can be mediated by floating gates [67, 68], schematically depicted in Fig. 4 in green.

Inductive coupling.— Inductive coupling via the superconducting loops is described by a term $\hat{H}_L = L \hat{I}_1 \hat{I}_2$ where $\hat{I}_j = \frac{2e}{\hbar} \frac{d\hat{H}_j}{d\phi_j}$ is the supercurrent operator in the loop and L the mutual inductance. However, the inductive coupling is not well-suited for our qubit design because at the phase sweet spot $\phi = \pi$, the derivatives, and thereby the inductive coupling, are zero. Moreover, around $\phi = \pi$, the coupling is proportional to $\tau \sin \eta$ [see Eq. (13)] and, thus, suppressed in the weak tunneling regime $|\eta| \ll 1$. It therefore requires strong tunneling between the dots to give a significant contribution.

III. PARAMETER NOISE

In this section, we quantify the susceptibility of the parity qubit to noise around the sweet spot. We use Fermi's golden rule and the Bloch-Redfield approximation to determine depolarization and dephasing rates. We use lowest-order perturbation theory for the qubit frequency ω_0 as a function of the fluctuating parameters. Here we focus on the relevant noise parameters. A dis-

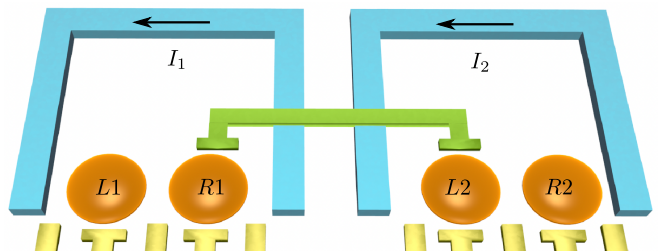


Figure 4. Device sketch for two-qubit gates: Two fermion-parity qubits 1, 2 can be coupled inductively or by a floating gate (green) mediating capacitive between quantum dots of distinct qubits.

discussion including fluctuations in all system parameters is contained in App. C.

We include terms coupling to the local spin,

$$\hat{H}_\nu^B = \sum_\sigma s_\sigma B_{z,\nu} \hat{n}_{\sigma\nu} + \left[(B_{x,\nu} - iB_{y,\nu}) \hat{c}_{\uparrow\nu}^\dagger \hat{c}_{\downarrow\nu} + \text{H.c.} \right], \quad (6)$$

with $s_\sigma = \pm 1$ for $\sigma = \uparrow, \downarrow$, which describes Zeeman coupling to magnetic fields as well as spin-spin exchange coupling to a nuclear spin bath. We further include spin-orbit coupling, which replaces the tunneling term in Eq. (3),

$$\hat{H}_T^{\text{SOC}} = \tau e^{i\phi} \left[\hat{c}_{\uparrow L}^\dagger, \hat{c}_{\downarrow L}^\dagger \right] e^{i\theta \vec{n} \cdot \vec{\sigma}} \begin{pmatrix} \hat{c}_{\uparrow R} \\ \hat{c}_{\downarrow R} \end{pmatrix} + \text{H.c.} \quad (7)$$

with the vector of Pauli matrices $\vec{\sigma} = (\sigma_x, \sigma_y, \sigma_z)^T$ in spin space. The matrix $e^{i\theta \vec{n} \cdot \vec{\sigma}}$ describes a rotation of the electron's spin by an angle θ around the axis \vec{n} as they tunnel from the right to left dot. For $\theta = 0$, the spin-orbit coupling is zero and Eq. (3) is recovered. The axis \vec{n} is called the spin-orbit direction. By choosing the spin quantization axis in both quantum dots to be aligned with \vec{n} , the spin-orbit coupling becomes diagonal, $\tau e^{i\theta \sigma_z}$. We choose this basis for the following, keeping in mind that the Zeeman fields are now given with respect to this basis, *i.e.* B_z points parallel to the spin-orbit axis \vec{n} .

In the presence of Zeeman fields, the angle η determining the qubit eigenstates and operating regimes (as defined in Eq. (4)) is modified,

$$\tan \eta_{\sigma,\lambda} = \frac{2\tau}{(U_R - U_L)/2 + s_\sigma(B_{zL} - B_{zR}) + s_\lambda(\Gamma_R - \Gamma_L)} \quad (8)$$

where $s_\lambda = \pm 1$ for $\lambda = g, u$. Equation (4) is recovered from Eq. (8) for $B_{zL} = B_{zR}$ and $\lambda = u$, see Sec. II B [69].

Dephasing and relaxation rates.— Assuming the computational qubit subspace to be decoupled from the remaining states governed by $\hat{H}(t)$ at any time t , the dephasing rate Γ_φ^χ due to a noisy, linearly coupled parameter χ is given in Bloch-Redfield theory as [49, 64]

$$\Gamma_\varphi^\chi = \pi \left(\frac{\partial \omega_0}{\partial \chi} \right)^2 S_\chi(\omega \rightarrow 0). \quad (9)$$

This presupposes that the noise spectral density

$$S_\chi(\omega) = \int_{-\infty}^{\infty} d\tau \langle \chi(0)\chi(\tau) \rangle e^{-i\omega\tau} \quad (10)$$

is regular near $\omega \approx 0$ up to frequencies of order of Γ_φ , where $\langle \chi(0)\chi(\tau) \rangle$ is the autocorrelation function of the fluctuating parameter χ with respect to its underlying statistical distribution.

The relaxation rate Γ_{rel}^χ is given in Fermi's golden rule [49, 64],

$$\Gamma_{\text{rel}}^\chi(\omega_0) = \frac{\pi}{2\hbar^2} \left| \langle + | \frac{d\hat{H}}{d\chi} | - \rangle \right|^2 S_\chi(\omega_0). \quad (11)$$

Similarly, the excitation rate is given by $\Gamma_{\text{exc}}^\chi(\omega_0) = \Gamma_{\text{rel}}^\chi(-\omega_0)$. Both processes contribute to the depolarization rate $\Gamma_1^\chi(\omega_0) = \Gamma_{\text{rel}}^\chi(\omega_0) + \Gamma_{\text{exc}}^\chi(\omega_0)$. At temperatures $k_B T \ll \hbar\omega_0$, the excitation rate $\Gamma_{\text{exc}}^\chi(\omega_0)$ is exponentially suppressed [49].

Level energy fluctuations.— Electric field fluctuations can couple to the level energy ε_ν of the quantum dots. To quantify their effect, we calculate the qubit frequency, $\hbar\omega_0^{(2)} = E_+^{(2)} - E_-^{(2)}$, to second order in the detuning of the level energy ε_ν away from the sweet spot,

$$\begin{aligned} \hbar\omega_0^{(2)} = \hbar\omega_0^{(0)} &+ \left(\frac{(\varepsilon_L + \frac{U_L}{2})^2}{2\Gamma_L} - \frac{(\varepsilon_R + \frac{U_R}{2})^2}{2\Gamma_R} \right) \cos \eta_{\sigma,u} \\ &- \left(\frac{\varepsilon_L + \frac{U_L}{2}}{2\Gamma_L} - \frac{\varepsilon_R + \frac{U_R}{2}}{2\Gamma_R} \right)^2 \tau \sin \eta_{\sigma,u}. \end{aligned} \quad (12)$$

The first correction arises from the quadratic dependence of the energy of the local even parity states of the individual dots on the level energy $\varepsilon_\nu + U_\nu/2$ around the sweet spot. The second correction describes a modification of the tunneling between these states due to the change of the Andreev bound state superposition by detuning ε_ν . In Eq. (12), we neglected a term describing second-order processes involving high-energy states $|g\rangle_\nu$ with a symmetric superposition of $|0\rangle_\nu$ and $|2\rangle_\nu$, see App. C for the full result. These states are separated from the qubit subspace by an energy difference of the order of $2\Gamma_\nu$.

The matrix element $\langle + | \frac{d\hat{H}}{d\varepsilon_\nu} | - \rangle = 0$ at the sweet spot. Thus we have $\Gamma_{\text{rel}}^{\varepsilon_\nu} = 0$ independent of the tunneling strength. Both the Bloch-Redfield dephasing rate and relaxation rate are zero at the sweet spot, $\varepsilon_\nu + U_\nu/2 = 0$ and $\phi = \pi$. We note that due to the quadratic dependence of the spectrum on the level energy ε_ν , there are higher-order contributions to the dephasing that are not captured by the Bloch-Redfield dephasing rate. These contributions however depend on the detailed form of the noise power spectral density and the time scale. Corresponding expressions can be found in Ref. [49].

Phase fluctuations.— The phase difference between the superconductors can fluctuate due to magnetic flux variations. To second order in the superconducting phase difference, the qubit frequency can be written as

$$\hbar\omega_0^{(2)} = \hbar\omega_0^{(0)} - \frac{\delta\phi^2}{4} \tau \sin \eta_{\sigma,u}. \quad (13)$$

Also here, we neglected a term describing second-order processes via the high-energy states $|g\rangle_\nu$, *c.f.* App. C. At the sweet spot $\varepsilon_\nu + U_\nu/2 = 0$ and $\phi = \pi$, also the matrix element $\langle + | \frac{d\hat{H}}{d\phi} | - \rangle = 0$, such that both Bloch-Redfield dephasing and the relaxation rate in Fermi's golden rule are zero.

Magnetic field fluctuations.— Fluctuating magnetic fields coupling to the electron spin include Zeeman coupling to external magnetic fields as well as spin-spin exchange interaction with the nuclear spin bath. Magnetic

fields along the spin-orbit axis have a linear contribution to the qubit frequency

$$\hbar\omega_0^{(1)} = \hbar\omega_0^{(0)} + s_\sigma(B_{z,L} - B_{z,R}) \cos \eta_{\sigma,u}. \quad (14)$$

This linear contribution is large for weak tunneling $|\eta_{\sigma,u}| \ll 1$, but goes to zero for strong tunnel coupling with $|\cot \eta_{\sigma,u}| \ll 1$. The relaxation rate $\Gamma_{\text{rel}}^{B_{z,\nu}} = \frac{\pi}{8\hbar^2} \sin^2 \eta_{\sigma,u} S_{B_{z,\nu}}(\omega_0)$ behaves oppositely: It is large for strong tunneling, but approaches zero for weak tunneling with $|\tan \eta_{\sigma,u}| \ll 1$.

Magnetic field fluctuations perpendicular to the spin-orbit direction induce transitions between the two spin sectors. Choosing one of the spin sectors as the computational space, these fluctuations would take the qubit out of the computational space. This can be avoided by applying an external Zeeman field B_z^{ext} . Ideally, this Zeeman field should be aligned with the spin-orbit direction \vec{n} to avoid spin-flipping processes from the spin-orbit coupling. Then, fluctuations in the orthogonal directions enter only to second order,

$$\hbar\omega_0^{(2)} = \hbar\omega_0^{(0)} - \frac{\delta B_x^2}{(B_z^{\text{ext}})^2} \frac{\tau \sin(\eta_{\sigma,u}) \sin^2 \theta}{1 - \tau^2 (\sin \eta_{\sigma,u})^{-2} (B_z^{\text{ext}})^{-2}}, \quad (15)$$

and similarly for B_y . This dephasing contribution decreases quadratically with the applied magnetic field and requires spin-orbit coupling, as expressed by the proportionality $\sin^2 \theta$ to the spin-orbit angle θ . Also here, the perpendicular fluctuations do not contribute to the relaxation rate in Fermi's golden rule, $\Gamma_{\text{rel}}^{B_x} = 0$.

Remaining parameters.— While the parity qubit is linearly protected against fluctuations in the level energies and the magnetic flux, fluctuations in other parameters can affect qubit performance. Fluctuations of local parameters of one of the dots, such as the charging energy U_ν and the induced pairing Γ_ν , contribute to the dephasing rate with a term proportional to $\sin^2(\eta_{\sigma,u})$ and to the relaxation rate proportional to $\cos^2(\eta_{\sigma,u})$. Fluctuations in the tunneling strength τ enter oppositely: They contribute to the dephasing rate proportional to $\cos^2(\eta_{\sigma,u})$ and to the relaxation rate proportional to $\sin^2(\eta_{\sigma,u})$.

Furthermore, a mutual charging energy $U_{\text{LR}} \sum_{\sigma,\sigma'} \hat{n}_{\sigma L} \hat{n}_{\sigma' R}$ modifies the system Hamiltonian in the odd fermion-parity subspace by replacing $U_\nu \rightarrow U_\nu + 2U_{\text{LR}}$. Accounting for the modified sweet spot, fluctuations in U_{LR} enter only to second order in the qubit frequency by detuning the system from the sweet spot as described by Eq. (12).

Beyond the decoherence channels discussed here, the depolarization rate of our proposed qubit is lower bounded by the fermion-parity lifetime of the individual quantum dots.

IV. COMPARISON TO OTHER QUBIT REALIZATIONS

Semiconductor spin qubit.— An common type of

single-electron qubits in semiconductors are spin qubits [70]. This type of qubits are vulnerable to magnetic fluctuations created by the nuclei spins in the host material, which is the reason why efforts are now focused on (possibly isotopically purified) silicon or germanium based dots [71–73]. One complication with spin qubits is that their spin state cannot be directly manipulated with electric fields, but instead requires oscillating magnetic fields, spin-orbit coupling, or gradient in the magnetic field. In our proposal, local magnetic fields couple to the states with odd fermion parity. We can reduce the effect of this coupling: (i) by applying a magnetic field larger than the local fluctuations, or (ii) by increasing the tunnel coupling of the quantum dots such that the qubit states are superpositions of $|L\rangle$ and $|R\rangle$ [see discussion around Eqs. (14) and (15)]. Moreover, our proposed gates use electrical control without the need for spin-orbit coupling or gradients in the magnetic field.

Andreev and Andreev spin qubits.— In superconductors, coherent control of single fermionic quasiparticles in Andreev bound states has been demonstrated in “Andreev qubits” where the computational states are given by the occupation of spin-degenerate Andreev bound states [18, 19]. Further experiments on “Andreev spin qubits” demonstrated coherent manipulation of the spin 1/2 degree of freedom of a quantum dot with odd fermion parity in contact to superconductors [20, 21]. These experiments have been performed in aluminum-based structures where relatively long parity and T_1 lifetimes were observed, while the dephasing times were shorter [18–20, 58]. Our proposal can be considered as a tuned double-dot version of these experiments.

Pairs of quantum dots coupled to superconductors.— Recently, other proposals for qubits in pairs of quantum dots coupled to superconductors have appeared. Ref. 74 discusses two quantum dots coupled to a single superconducting island. By tuning the level energies of the quantum dots, a similar charge-insensitive sweet spot can be reached. An ongoing project [75] studies a pair of quantum dots in a Josephson junction where the qubit is encoded in Yu-Shiba-Rusinov states.

Majorana qubit.— Our proposal shares two essential properties with topological Majorana qubits [76–78], namely that the information is encoded in the fermion parity of localized modes and that the information is separated from the electronic charge. However, there are fundamental differences. In Majorana qubits, the quantum information is stored in spatially separated Majorana bound states, where a pair of Majorana bound states composes a single complex fermion. Individual Majorana bound states are chargeless quasiparticles. Dephasing of quantum information stored in Majorana bound states due to local fluctuations occurs only via modifications of the hybridization to other Majorana bound states (which is exponentially suppressed in their distance in the topological case). In contrast, in our proposal the quantum dots are fine-tuned to a sweet spot with zero charge dipole moment. In spirit, our proposal is thus related to two-dot

Kitaev chain proposals [29, 37, 79]. However, this so-called "poor man's" Majorana system has qubit states defined by the total parity of two dots (and therefore needs four dots to make a workable qubit), whereas for our proposal the qubit states are defined by local parity (and therefore two dots are sufficient).

V. EXPERIMENTAL PLATFORMS

We expect that our qubit proposal can be implemented in current superconductor-semiconductor platforms. One of the most promising platforms for demonstration purposes are aluminum superconductors deposited on top of an electron gas formed in a III-V semiconductor such as indium-arsenide [80–83] or indium antimony [28, 84, 85]. This platform hosts very clean interfaces between the Al superconductor and the indium-arsenide electron gas such that electrostatically tunable hopping rates Γ_ν from zero to larger than the superconducting gap $\Delta \approx 0.2\text{meV}$ of Al as well as quantum dots with level spacing much larger than the hopping rates to justify the single level approximation are achievable [86]. In this platform, all of the requirements for our proposal have been demonstrated: Coherent manipulation of Andreev bound states and electron spins in quantum dots [18–21], fermion-parity initialization [58, 59], and good control of the hybridization of Andreev bound states in quantum dots [28]. Furthermore, this platform can be integrated with superconducting circuits [58], which enhances the range of possibilities for qubit addressing and readout, and interfaces with other superconducting qubits. A challenge in this platform for our qubit proposal is the nuclear spin bath, which causes dephasing by inducing fluctuating spin-spin exchange fields in the quantum dots via the Overhauser effect [87]. Therefore, this platform cannot be expected to be viable as a long coherence time qubit, but is well-suited for demonstration experiments. Another possible platform in III-V semiconductors is gallium arsenide with niobium nitride superconductors [88], which realizes high-mobility electron gases with very good electrostatic tunability.

A promising platform with higher coherence are group IV semiconductors such as germanium / silicon germanium heterostructures which make good interfaces with aluminum [73, 89] or germanosilicide [90] superconductors. In group IV semiconductors, most isotopes have zero nuclear spin which suppresses exchange field fluctuations from the Overhauser effect. In carbon-based materials, quantum dots have been realized in Bernal-stacked bilayer graphene [91], where long-lived valley degrees of freedom have been reported [92]. Bilayer graphene itself can turn superconducting [93] by electrostatic gating, and the superconductivity can be enhanced by coupling to a tungsten diselenide monolayer [94]. Alternatively, graphene can be interfaced with a niobium nitride superconductor by etching the graphene and depositing the superconductor [95, 96].

VI. CONCLUSIONS AND DISCUSSIONS

We have proposed a qubit where quantum information is encoded in the fermion parity of two quantum dots constituting a weak link in a superconducting loop. The qubit states are defined by the fermion number parity of the two quantum dots. By electrostatic tuning to a sweet spot, the quantum dots have the same electric charge, independently of their fermion parity. Thereby, the qubit states are protected from dephasing to first order in fluctuations of the electric field that lead to variations of the quantum dot level energy much smaller than the induced superconducting correlations. By tuning the tunneling strength between the quantum dots, the encoded quantum information is further protected towards relaxation (weak tunneling) or dephasing (strong tunneling) induced by environmental fluctuations coupling to individual quantum dots, including electric and magnetic fields, and nuclear spins. The reduced sensitivity towards local noise may mediate the main decoherence sources in qubits in quantum dot-superconductor heterostructures, such as Andreev [18, 19] and Andreev spin qubits [20, 21] [see Sec. IV]. Strong tunneling increases the dephasing due to fluctuations of the tunneling amplitude, which could be reduced by lowering the coupling between gate voltage and tunneling strength.

The fermion-parity qubit is controllable with electric gates to perform single- and two-qubit gates, as well as initialization and read-out. The qubit states are well separated from the nearest non-computational states by an energy difference of the order of the induced pairing potential $2\Gamma_\nu$, which permits fast gate operations while avoiding population of non-computational states. Taking aluminium as a host superconductor with gap $\Delta \approx 0.2\text{meV}$ and estimating $\Gamma_\nu \approx \Delta/4 = 2\pi\hbar \times 12\text{GHz}$, we expect that single-qubit gates can be achieved on a nanosecond scale.

Future theoretical directions of this work could address how large charging energy $U_\nu \gg \Delta$, Γ_ν or induced pairing strength $\Gamma_\nu \gg \Delta$ modifies the qubit spectrum and decoherence properties in detail. We expect that the qualitative features of our proposal persist for large charging energy, with quantitative modifications as the even-parity bound states become singlets composed of an electron on the dot and a quasiparticle from the superconductor [1–3, 43, 44].

An experimental realization of our proposal would demonstrate encoding of quantum information in the fermionic parity degree of freedom separated from its electric charge. This property is shared by the topological Majorana qubits and is an essential element in their anticipated decoupling of the encoded quantum information from the environmental noise. While topological Majorana qubits [76–78] have proven difficult to realize, our proposal uses currently available technology. We hope our proposal inspires experimental realization and further studies on how superconductivity can decouple quantum information from the environment.

VII. ACKNOWLEDGEMENTS

We thank Anasua Chatterjee, Ferdinand Kuemmeth, Charles M. Marcus, Jens Paaske, and Gorm Ole Stefensen for discussions. We acknowledge support from the Danish National Research Foundation, the Danish Council for Independent Research | Natural Sciences, the European Research Council (Grant Agreement No. 856526), Spanish CM ‘‘Talento Program’’ (project No. 2022-T1/IND-24070), the Swedish Research Council (Grant Agreement No. 2020-03412), and NanoLund. This project has received funding from the European Union’s Horizon 2020 research and innovation program under the Marie Skłodowska-Curie grant agreement No. 10103324 and funded by the European Union under the Grant Agreement no. 101063135.

Appendix A: Validity of the effective Hamiltonian

The Hamiltonian \hat{H}_ν defined in Eq. (2) is an accurate description for individual quantum dots when the gap Δ in the surrounding superconductor is large, $\Delta \gg \Gamma_\nu, U_\nu$. At large charging energy, $U_\nu \gg \Delta, \Gamma_\nu$, an accurate description of the individual quantum dots coupled to superconductors requires to take the superconductors and the hopping to them explicitly into account [17, 31, 38, 44, 56]. In comparison to the description using \hat{H}_ν where coupling to the superconductors is included in lowest-order perturbation theory via Γ_ν , the even-parity bound states get modified: Double-occupation of the quantum dot is avoided by forming a singlet with a quasiparticle from the superconductor. This leads to a renormalization of the even-fermion-parity bound state energies [44]. We expect that while changing the quantitative details, the qualitative features of our results should persist in this limit: A sweet spot where both fermion parity sectors of a quantum dot have the same mean charge can also be reached for large charging energy.

Appendix B: Rabi driving at the sweet spot

Rabi transitions of the qubit states can also be achieved by driving the level energy ε_ν at the sweet spot. In this regime, we have to account for the quadratic dependence of the qubit frequency on the detuning of the level energy around the sweet spot, $\hbar\omega_0(\varepsilon_\nu) = \hbar\omega_0(-U_\nu/2) + \frac{1}{2} \frac{\partial^2 \omega_0}{\partial \varepsilon_\nu^2} (\varepsilon_\nu + U_\nu/2)^2 + \mathcal{O}((\varepsilon_\nu + U_\nu/2)^4)$, where the factor $\frac{1}{2} \frac{\partial^2 \omega_0}{\partial \varepsilon_\nu^2}$ can be determined from perturbation theory, see App. C for an explicit expression. Due to the quadratic dependence of the low-energy Hamiltonian projected on the qubit subspace in the driven parameter $\varepsilon_\nu(t) = -U_\nu/2 + \delta\varepsilon_\nu \cos(\Omega t)$, the drive enters the qubit subspace as $\frac{1}{2} \frac{\partial^2 \omega_0}{\partial \varepsilon_\nu^2} (\varepsilon_\nu(t) + U_\nu/2)^2 = \frac{1}{4} \frac{\partial^2 \omega_0}{\partial \varepsilon_\nu^2} \delta\varepsilon_\nu^2 [1 + \cos(2\Omega t)]$ with doubled frequency. For small driving am-

plitudes, $\frac{1}{4} \frac{\partial^2 \omega_0}{\partial \varepsilon_\nu^2} \delta\varepsilon_\nu^2 \ll \hbar\omega_0$, the driving frequency Ω needs to be set to half of the qubit frequency at the sweet spot, $\Omega = \omega_0/2$ to achieve complete population transfer. For finite driving amplitudes, $\frac{1}{4} \frac{\partial^2 \omega_0}{\partial \varepsilon_\nu^2} \delta\varepsilon_\nu^2 \gtrsim \hbar\omega_0$, the qubit frequency $\tilde{\omega}_0 = \frac{1}{T} \int_0^T dt \omega_0[\varepsilon_\nu(t)] = \hbar\omega_0(-U_\nu/2) + \frac{1}{4} \frac{\partial^2 \omega_0}{\partial \varepsilon_\nu^2} \delta\varepsilon_\nu^2$ averaged over one period of the drive $T = \frac{2\pi}{\Omega}$ deviates from the non-driven value ω_0 such that the driving frequency needs to be corrected as $\Omega = \frac{1}{2} \tilde{\omega}_0 = \frac{1}{2} \omega_0 + \frac{1}{8} \frac{\partial^2 \omega_0}{\partial \varepsilon_\nu^2} \delta\varepsilon_\nu^2$ to allow complete population transfer. The sweet spot driving is demonstrated in Fig. 3(b). A similar result also allows driving of the phase difference ϕ at the sweet spot $\phi = \pi$ to perform qubit rotations.

Appendix C: Perturbation theory and decoherence rates

Here we give the full result of the second-order perturbation theory for the qubit frequency around the sweet spot $\varepsilon_\nu = -U_\nu/2$ and at the operating point $\phi = \pi$. These results are employed to calculate the Bloch-Redfield dephasing rates and depolarization rates from Eqs. (9) and (11).

1. Diagonalization at the sweet spot

The full qubit Hamiltonian including spin-orbit coupling and Zeeman fields,

$$\hat{H} = \sum_\nu (\hat{H}_\nu + \hat{H}_\nu^B) + \hat{H}_T^{\text{soc}}, \quad (\text{C1})$$

is conveniently diagonalized in the eigenbasis of proximitized dots \hat{H}_ν ,

$$|\lambda_\nu\rangle_\nu = \frac{|0\rangle + (\sinh(\xi_\nu) + s_{\lambda_\nu} \cosh(\xi_\nu)) c_{\uparrow\nu}^\dagger c_{\downarrow\nu}^\dagger |0\rangle}{N_{\lambda_\nu}} \quad (\text{C2})$$

with labels $\lambda_\nu = \text{g, u}$ as in Sec. II B, $N_{\lambda_\nu} = \sqrt{2 \cosh \xi_\nu (\cosh \xi_\nu + s_{\lambda_\nu} \sinh \xi_\nu)}$, $\sinh \xi_\nu = \frac{2\varepsilon_\nu + U_\nu}{2\Gamma_\nu}$ and energy $E_{\lambda_\nu} = \Gamma_\nu (\sinh \xi_\nu + s_{\lambda_\nu} \cosh \xi_\nu)$.

In the eigenbasis of proximitized dots \hat{H}_ν as given in Eq. (C2), the Hamiltonian within a spin sector σ can be written in matrix form,

$$\hat{H}_\sigma = \begin{pmatrix} \varepsilon_{\sigma L} + E_{\text{gR}} & 0 & \tau e^{i\sigma\theta} f_{\text{gg}} & \tau e^{i\sigma\theta} f_{\text{gu}} \\ 0 & \varepsilon_{\sigma L} + E_{\text{uR}} & \tau e^{i\sigma\theta} f_{\text{ug}} & \tau e^{i\sigma\theta} f_{\text{uu}} \\ \text{H.c.} & & \varepsilon_{\sigma R} + E_{\text{gL}} & 0 \\ & & 0 & \varepsilon_{\sigma R} + E_{\text{uL}} \end{pmatrix} \quad (\text{C3})$$

acting on the basis $(\hat{c}_{\sigma L}^\dagger |g\rangle_R, \hat{c}_{\sigma L}^\dagger |u\rangle_R, \hat{c}_{\sigma R}^\dagger |g\rangle_L, \hat{c}_{\sigma R}^\dagger |u\rangle_L)^\text{T}$,

where $\varepsilon_{\sigma\nu} = \varepsilon_\nu + s_\sigma B_{z,\nu}$ and

$$f_{\lambda_R\lambda_L} = \frac{e^{i\phi/2}}{N_{\lambda_R}N_{\lambda_L}} \quad (\text{C4})$$

$$- \frac{s_{\lambda_R}s_{\lambda_L}e^{-i\phi/2}}{N_{\lambda_R}N_{\lambda_L}} \left(\cosh(s_{\lambda_L}\xi_L + s_{\lambda_R}\xi_R) \right. \\ \left. + \sinh(s_{\lambda_L}\xi_L + s_{\lambda_R}\xi_R) \right)$$

At the sweet spot $\xi_L = \xi_R = 0$, the function $f_{\lambda_R\lambda_L}$ simplifies as $f_{\lambda\lambda}^{(0)} = i \sin \frac{\phi}{2}$ and $f_{\lambda\lambda}^{(0)} = \cos \frac{\phi}{2}$ where $\bar{g}/\bar{u} = u/g$. Thus, the tunnel-coupling of the quantum dot states can be controlled by the phase-bias ϕ : At $\phi = 0$, the low-energy state $|u\rangle_L$ of the left dot is coupled to the high-energy state $|g\rangle_R$ of the right dot, and vice versa. At $\phi = \pi$, the low-energy states $|u\rangle_L$, $|u\rangle_R$ and high-energy states $|g\rangle_L$, $|g\rangle_R$ are coupled with each other. The perpendicular components of the Zeeman field $B_{x,\nu}$, $B_{y,\nu}$ remain unaffected by this basis transformation.

At the sweet spot, for $B_{x,\nu} = B_{y,\nu} = 0$, and at $\phi = \pi$, the eigenstates of the full Hamiltonian \hat{H} are,

$$|\sigma, \lambda, -\rangle = \sin \frac{\eta_{\sigma,\lambda}}{2} \hat{c}_{\sigma L}^\dagger |\lambda\rangle_R + ie^{-is_\sigma\theta} \cos \frac{\eta_{\sigma,\lambda}}{2} \hat{c}_{\sigma R}^\dagger |\lambda\rangle_L$$

$$|\sigma, \lambda, +\rangle = \cos \frac{\eta_{\sigma,\lambda}}{2} \hat{c}_{\sigma L}^\dagger |\lambda\rangle_R - ie^{-is_\sigma\theta} \sin \frac{\eta_{\sigma,\lambda}}{2} \hat{c}_{\sigma R}^\dagger |\lambda\rangle_L \quad (\text{C5})$$

with energy

$$E_{\sigma,\lambda,\rho}^{(0)} = \frac{-(U_R + U_L)/2 + s_\sigma(B_{zL} + B_{zR}) + s_\lambda(\Gamma_R + \Gamma_L)}{2} \\ + \rho \frac{\tau}{\sin \eta_{\sigma,\lambda}}, \quad (\text{C6})$$

with $\rho = \pm$ labeling the corresponding eigenstate and the superscript (0) indicates the sweet spot. The angle $\eta_{\sigma,\lambda}$ is given in Eq. (8). It determines the operating regime: For small $|\eta_{\sigma,u}| \ll \pi/2$ (weak tunneling), the eigenstates Eqs. (C5) are localized either left or right, while for large $|\eta_{\sigma,u}| \approx \pi/2$ (strong tunneling), the eigenstates are bonding and anti-bonding superpositions between left and right.

The two qubit states are given by the two lowest energy eigenstates of the system within a spin sector σ , $|\sigma, u, -\rangle$ and $|\sigma, u, +\rangle$. The qubit eigenfrequency is

$$\hbar\omega_0^{(0)} = E_{\sigma,u,+}^{(0)} - E_{\sigma,u,-}^{(0)} = 2 \frac{\tau}{\sin \eta_{\sigma,u}}. \quad (\text{C7})$$

For Zeeman fields (and fluctuations thereof) much smaller than $\hbar\omega_0^{(0)}$, the system can be operated in the spin degenerate regime. For sizeable fluctuations of the Zeeman fields, it is advantageous to apply an external magnetic field $B_{z\nu}^{\text{ext}}$ much larger than the variance of the fluctuations to suppress spin flips. Differences in the electronic g -factor in the two quantum dots g_ν lead different resulting Zeeman fields $B_{z\nu}^{\text{ext}}$.

2. Deviations from the operating regime

Here we summarize the results for the lowest order corrections to the qubit spectrum due to perturbations in the system parameters away from the operating point at the sweet spot $\varepsilon_\nu = -U_\nu/2$ and $\phi = \pi$.

Detuning ε_ν .— We calculate the energy difference $\hbar\omega_0^{(2)} = E_{\sigma,u,+}^{(2)} - E_{\sigma,u,-}^{(2)}$ of the qubit states to second order in the detuning,

$$\hbar\omega_0^{(2)} = \hbar\omega_0^{(0)} + \frac{\Gamma_L\xi_L^2 - \Gamma_R\xi_R^2}{2} \cos \eta_{\sigma,u} \quad (\text{C8}) \\ - \left(\frac{\xi_L - \xi_R}{2} \right)^2 (1 + 2\xi_{\sigma,u}^2) \tau \sin \eta_{\sigma,u}$$

where $\xi_\nu = \text{arsinh} \frac{2\varepsilon_\nu + U_\nu}{2\Gamma_\nu} \approx \frac{2\varepsilon_\nu + U_\nu}{2\Gamma_\nu}$ and $\xi_{\sigma,\lambda} = \frac{1}{\Gamma_R + \Gamma_L} \frac{\tau}{\sin \eta_{\sigma,\lambda}}$. The first correction arises from the quadratic dependence of the energy E_{λ_ν} of the local even parity states of the individual dots. The second correction describes a modification of the tunneling between these states due to their dependence of the Andreev bound state wavefunction (Eq. (C2)) on the level energy ε_ν . The term proportional to $\xi_{\sigma,u}$ describes second-order processes involving the symmetric even-fermion-parity bound states $\lambda_\nu = g$ at high energy $\lambda_\nu\Gamma_\nu$ at the sweet spot. The above result is furthermore expanded to lowest order in $\xi_{\sigma,\lambda}$, which is small $\xi_{\sigma,\lambda} \ll 1$ when the qubit states $\lambda_\nu = u$ are well separated from the high-energy states $\lambda_\nu = g$. Neglecting the coupling to the symmetric even-fermion-parity bound states ($\xi_{\sigma,u} \rightarrow 0$) reproduces Eq. (12).

Phase difference ϕ .— Similarly, the variations of the phase difference $\phi = \pi + \delta\phi$ away from the operating point $\phi = \pi$ modify the qubit frequency as

$$\hbar\omega_0^{(2)} = \hbar\omega_0^{(0)} - \frac{\delta\phi^2}{4} (1 + 2\xi_{\sigma,u}^2) \tau \sin \eta_{\sigma,u} \quad (\text{C9})$$

which, again, is expanded to second order in $\xi_{\sigma,\lambda}$. Setting $\xi_{\sigma,u} \rightarrow 0$ reproduces Eq. (13).

Tunneling strength τ .— Variations in the magnitude of the tunneling amplitude $\tau \rightarrow \tau + \delta\tau$ enter linearly in the qubit frequency,

$$\hbar\omega_0^{(1)} = \hbar\omega_0^{(0)} + \delta\tau \sin \eta_{\sigma,u}. \quad (\text{C10})$$

Charging energy U_ν .— Fluctuations in the charging energy U_ν on either dot modify the qubit frequency to linear order,

$$\hbar\omega_0^{(1)} = \hbar\omega_0^{(0)} + \left(\frac{\delta U_R}{2} - \frac{\delta U_L}{2} \right) \cos \eta_{\sigma,u}. \quad (\text{C11})$$

Induced pairing potential Γ_ν .— At the sweet spot, fluctuations in the induced pairing strength $\Gamma_\nu \rightarrow \Gamma_\nu + \delta\Gamma_\nu$ modify only the diagonal elements of the Hamiltonian. The offdiagonal terms remain unchanged as $\xi_\nu = 0$. The energy depends linearly on the perturbation,

$$\hbar\omega_0^{(1)} = \hbar\omega_0^{(0)} + (\delta\Gamma_L - \delta\Gamma_R) \cos \eta_{\sigma,u}. \quad (\text{C12})$$

Zeeman fields \vec{B}_ν .— Dephasing and depolarization due to Zeeman field fluctuations are discussed around Eqs. (14) and (15) in the main text.

Spin-orbit coupling.— Spin-orbit coupling enters the Hamiltonian via the tunneling term Eq. (7). Without Zeeman fields, or for Zeeman fields pointing only along the spin-orbit direction \vec{n} , the spin-orbit coupling does not modify the spectrum. The spin orbit angle θ enters only in the perturbative corrections due to orthogonal fluctuations of the Zeeman field [see Eq. (15)].

3. Dephasing and depolarization

We derive Bloch-Redfield dephasing rates and depolarization rates using Eqs. (9) and (11) from the main text.

Detuning ε_ν .— Using Eq. (12), the dephasing rate due to fluctuations in the detuning ε_ν around the sweet spot is

$$\frac{2\hbar^2}{\pi S_\varepsilon(\omega \rightarrow 0)} \Gamma_\varphi^{\varepsilon_\nu} = \left(\xi_\nu \cos \eta_{\sigma,u} + \frac{\xi_L - \xi_R}{2\Gamma_\nu} (1 + 2\Xi_{\sigma,u}^2) \tau \sin \eta_{\sigma,u} \right)^2. \quad (\text{C13})$$

To compute the relaxation rate, we calculate at the sweet spot and $\phi = \pi$

$$\frac{d\hat{H}}{d\varepsilon_\nu} = \mathbb{1}_4 + \frac{\tau}{2\Gamma_\nu} \lambda_y \otimes \nu_x \quad (\text{C14})$$

where λ_l and ν_l , $l = 0, x, y, z$ are Pauli matrices in λ space and quantum dot space, respectively, and " \otimes " denotes the direct product. The matrix element $\langle + | \frac{d\hat{H}}{d\varepsilon_\nu} | - \rangle = 0$ due to orthogonality of the wavefunction and because the operator $\lambda_y \otimes \nu_x$ relates wavefunctions with opposite λ , while the two qubit states have the same $\lambda = -$. Thus we have

$$\Gamma_{\text{rel}}^{\varepsilon_\nu} = 0. \quad (\text{C15})$$

Both the Bloch-Redfield dephasing rate and relaxation rate are zero at the sweet spot $\xi_\nu = 0$ and $\phi = \pi$.

Phase difference ϕ .— The dephasing rate due to fluctuations in $\phi = \pi + \delta\phi$ is

$$\frac{2\hbar^2}{\pi S_\phi(\omega \rightarrow 0)} \Gamma_\varphi^\phi = \left(\frac{\delta\phi (1 + 2\Xi_{\sigma,u}^2) \tau \sin \eta_{\sigma,u}}{2} \right)^2. \quad (\text{C16})$$

With $\frac{d\hat{H}}{d\phi} = -\lambda_x \otimes \nu_x$ at $\phi = \pi$ we find $\langle + | \frac{d\hat{H}}{d\phi} | - \rangle = 0$ because the operator $\lambda_x \otimes \nu_x$ couples only states with opposite λ , such that

$$\Gamma_{\text{rel}}^\phi = 0. \quad (\text{C17})$$

Tunneling strength τ .— Fluctuations in the tunneling strength lead to a dephasing and relaxation rate,

$$\Gamma_\varphi^\tau = \frac{\pi}{\hbar^2} \sin^2 \eta_{\sigma,u} S_\tau(\omega \rightarrow 0) \quad (\text{C18})$$

$$\Gamma_{\text{rel}}^\tau = \frac{\pi}{2\hbar^2} \cos^2 \eta_{\sigma,u} S_\tau(\omega_0) \quad (\text{C19})$$

where we used that $d\hat{H}/d\tau_\sigma = -\lambda_0 \otimes \nu_y$ at $\phi = \pi$.

Charging energy U_ν .— Fluctuating charging energies U_ν on either dot result in dephasing and relaxation rates, to first order around the sweet spot $U_\nu = -2\varepsilon_\nu$,

$$\Gamma_\varphi^{U_\nu} = \frac{\pi}{4\hbar^2} \cos^2 \eta_{\sigma,u} S_{U_\nu}(\omega \rightarrow 0) \quad (\text{C20})$$

$$\Gamma_{\text{rel}}^{U_\nu} = \frac{\pi}{32\hbar^2} \sin^2 \eta_{\sigma,u} S_{U_\nu}(\omega_0). \quad (\text{C21})$$

where we used that $d\hat{H}/dU_{L/R} = \lambda_0 \otimes (\nu_0 \pm \nu_z)/4$.

Induced pairing strength Γ_ν .— The dephasing and relaxation rates due to fluctuating Γ_ν

$$\Gamma_\varphi^{\Gamma_\nu} = \frac{\pi}{\hbar^2} \cos^2 \eta_{\sigma,u} S_{\Gamma_\nu}(\omega \rightarrow 0) \quad (\text{C22})$$

$$\Gamma_{\text{rel}}^{\Gamma_\nu} = \frac{\pi}{8\hbar^2} \sin^2 \eta_{\sigma,u} S_{\Gamma_\nu}(\omega_0). \quad (\text{C23})$$

using $d\hat{H}/d\Gamma_{L/R} = \lambda_0 \otimes (\nu_0 \pm \nu_z)/2$.

Zeeman fields \vec{B} .— We again distinguish fluctuations B_z along the spin quantization axis in the two dots, and perpendicular fluctuations B_x , B_y . The spin quantization axis is either set by the direction of the spin-orbit coupling \vec{n} and/or the direction of an externally applied Zeeman field B_z^{ext} , see Sec. C2. Parallel fluctuations δB_z result in dephasing and relaxation rates

$$\Gamma_\varphi^{B_{z,\nu}} = \frac{\pi}{\hbar^2} \cos^2 \eta_{\sigma,u} S_{B_{z,\nu}}(\omega \rightarrow 0) \quad (\text{C24})$$

$$\Gamma_{\text{rel}}^{B_{z,\nu}} = \frac{\pi}{8\hbar^2} \sin^2 \eta_{\sigma,u} S_{B_{z,\nu}}(\omega_0). \quad (\text{C25})$$

In the presence of an externally applied Zeeman field much larger than the variance of the fluctuations of B_x and B_y , fluctuations in these components yield dephasing and relaxation rates

$$\Gamma_\varphi^{B_{x,\nu}} = \frac{\pi}{\hbar^2} \frac{4\delta B_x^2}{(B_z^{\text{ext}})^4} \left(\frac{\tau \sin \eta_{\sigma,u} \sin^2 \theta}{1 - \left(\frac{\tau}{B_z^{\text{ext}} \sin \eta_{\sigma,u}} \right)^2} \right)^2 S_{B_{x,\nu}}(\omega \rightarrow 0) \quad (\text{C26})$$

$$\Gamma_{\text{rel}}^{B_{x,\nu}} = 0. \quad (\text{C27})$$

The dephasing rate is zero in the absence of a bias $\delta B_x = 0$ and / or in the absence of spin-orbit coupling $\theta = 0$.

Relative dephasing of multiple qubits.— When operating all qubits at the sweet spot, the charge expectation value of all quantum dots is independent of their fermion parity. Therefore, any charge dipole or multipole moments between different qubits vanish as well, such that also a multi-qubit system remains linearly insensitive to fluctuations in the level energy. Similar arguments hold for the other parameters.

Appendix D: Pulse parameters

Here, we define the precise form and parameters for the pulses applied in Fig. 2 and 3 in the main text.

The pulses are of the form

$$f(t) = s(t; t_{\text{pulse}}, t_{\text{rise}}) \cos(\Omega t + \phi_0) \quad (\text{D1})$$

with the driving frequency Ω , pulse phase ϕ_0 and envelope function

$$s(t; t_{\text{pulse}}, t_{\text{rise}}) = \vartheta(t - t_{\text{pulse}}/2; t_{\text{rise}}) - \vartheta(t + t_{\text{pulse}}/2; t_{\text{rise}}) \quad (\text{D2})$$

setting the pulse duration t_p . The pulse is turned on smoothly over a rising time t_r using the smooth step function

$$\vartheta(t; t_{\text{rise}}) = \left(1 + \exp \left[\frac{t_{\text{rise}}}{t + t_{\text{rise}}/2} - \frac{t_r}{t_{\text{rise}}/2 - t} \right] \right)^{-1} \quad (\text{D3})$$

which is defined on the interval $-t_{\text{rise}}/2 < t < t_{\text{rise}}$. This smooth step function connects continuously in derivatives of all orders to a flat line $\vartheta(t) = 0$ for $t < -t_{\text{rise}}/2$ and $\vartheta(t) = 1$ for $t > t_{\text{rise}}/2$.

Weak tunneling, X_π rotation [Fig. 2(b)].— The pulse on the tunneling amplitude is of the form $\tau(t) = \tau + \delta\tau f(t)$ with amplitude $\delta\tau = 0.006\Gamma_L$, frequency $\Omega = \omega_0$, pulse time $t_{\text{pulse}} = 115h/\Gamma_L$ and rise time $t_{\text{rise}} = 10h/\Gamma_L$.

The ramp on the level energy ε_R is parameterized using the smooth step functions, $\varepsilon_R(t) = -U_R/2 + \delta\varepsilon_{R,\text{ramp}}(1 - s(t; t_{\text{pulse}} + t_{\text{ramp}} + t_{\text{rise}}, t_{\text{ramp}}))$ with $\delta\varepsilon_{R,\text{ramp}} = \Gamma_L$ and ramp time $t_{\text{ramp}} = 30h/\Gamma_L$. The pulse starts directly after the ramp is completed.

Weak tunneling, $X_{\pi/2}Z_{2\pi}X_{\pi/2}$ sequence of rotations [Fig. 2(c)].— The two consecutive pulses on the tunneling amplitude are performed with $\delta\tau = 0.006\Gamma_L$, frequency $\Omega = \omega_0$, pulse time $t_{\text{pulse}} = 60h/\Gamma_L$ and rise time $t_{\text{rise}} = 10h/\Gamma_L$. The pulses are separated by a waiting time $t_w = 7.75h/\Gamma_L$ and have the same phase ϕ_0 .

Weak tunneling, $X_{\pi/2}Z_{2\pi}X_{\pi/2}$ sequence of rotations [Fig. 2(d)].— Same parameters as in Fig. 2(c), except that the phase of the second pulse is shifted $\phi_0 \rightarrow \phi_0 + \pi$.

Strong tunneling, X_π rotation with detuned ε_R [Fig. 3(a)].— The pulse on the level energy ε_R is applied for a detuned $\varepsilon_R(t) = -U_R/2 + \delta\varepsilon_{\text{detune}} + \delta\varepsilon f(t)$, with detuning $\delta\varepsilon_{\text{detune}} = 0.2\Gamma_L$, pulse amplitude $\delta\varepsilon_R = 0.1\Gamma_L$, frequency $\Omega = \omega_0$, pulse time $t_{\text{pulse}} = 55h/\Gamma_L$ and rise time $t_{\text{rise}} = 10h/\Gamma_L$.

Strong tunneling, X_π rotation with by driving the level energy at the sweet spot [Fig. 3(a)].— The pulse to perform a X_π rotation by drive the level energy at the sweet spot is of the form $\varepsilon_R(t) = -U_R/2 + \delta\varepsilon f(t)$ with amplitude $\delta\varepsilon_R = 0.3\Gamma_L$, frequency $\Omega = \frac{1}{2}\omega_0 + \frac{1}{8}\frac{\partial^2\omega_0}{\partial\varepsilon_\nu^2}\delta\varepsilon_\nu^2 \approx 0.500214\omega_0$ [see App. B], pulse time $t_{\text{pulse}} = 50h/\Gamma_L$ and rise time $t_{\text{rise}} = 10h/\Gamma_L$.

-
- [1] L. Yu, *Acta. Phys. Sin.* **21**, 75 (1965).
 [2] H. Shiba, *Prog. Theor. Phys.* **40**, 435 (1968).
 [3] A. I. Rusinov, *Soviet Journal of Experimental and Theoretical Physics Letters* **9**, 85 (1969).
 [4] I. O. Kulik, *Soviet Journal of Experimental and Theoretical Physics* **30**, 944 (1969).
 [5] N. Hatter, B. W. Heinrich, M. Ruby, J. I. Pascual, and K. J. Franke, *Nat. Commun.* **6**, 1 (2015).
 [6] A. Jellinggaard, K. Grove-Rasmussen, M. H. Madsen, and J. Nygård, *Phys. Rev. B* **94**, 064520 (2016).
 [7] L. Hofstetter, S. Csonka, J. Nygård, and C. Schönberger, *Nature* **461**, 960 (2009).
 [8] R. S. Deacon, Y. Tanaka, A. Oiwa, R. Sakano, K. Yoshida, K. Shibata, K. Hirakawa, and S. Tarucha, *Phys. Rev. Lett.* **104**, 076805 (2010).
 [9] J.-D. Pillet, C. H. L. Quay, P. Morfin, C. Bena, A. L. Yeyati, and P. Joyez, *Nat. Phys.* **6**, 965 (2010).
 [10] J. Shen, S. Heedt, F. Borsoi, B. van Heck, S. Gazibegovic, R. L. M. Op het Veld, D. Car, J. A. Logan, M. Pendharkar, S. J. J. Ramakers, G. Wang, D. Xu, D. Bouman, A. Geresdi, C. J. Palmström, E. P. A. M. Bakkers, and L. P. Kouwenhoven, *Nat. Commun.* **9**, 1 (2018).
 [11] A. Pöschl, A. Danilenko, D. Sabonis, K. Kristjuhan, T. Lindemann, C. Thomas, M. J. Manfra, and C. M. Marcus, *Phys. Rev. B* **106**, L161301 (2022).
 [12] A. Banerjee, M. Geier, M. A. Rahman, D. S. Sanchez, C. Thomas, T. Wang, M. J. Manfra, K. Flensberg, and C. M. Marcus, *Phys. Rev. Lett.* **130**, 116203 (2023).
 [13] J. A. van Dam, Y. V. Nazarov, E. P. A. M. Bakkers, S. De Franceschi, and L. P. Kouwenhoven, *Nature* **442**, 667 (2006).
 [14] R. Delagrangé, R. Weil, A. Kasumov, M. Ferrier, H. Bouchiat, and R. Deblock, *Phys. Rev. B* **93**, 195437 (2016).
 [15] A. M. Whiticar, A. Fornieri, A. Banerjee, A. C. C. Drachmann, S. Gronin, G. C. Gardner, T. Lindemann, M. J. Manfra, and C. M. Marcus, *Phys. Rev. B* **103**, 245308 (2021).
 [16] D. Razmadze, R. S. Souto, L. Galletti, A. Maiani, Y. Liu, P. Krogstrup, C. Schrade, A. Gyenis, C. M. Marcus, and S. Vaitiekėnas, *Phys. Rev. B* **107**, L081301 (2023).
 [17] E. J. H. Lee, X. Jiang, M. Houzet, R. Aguado, C. M. Lieber, and S. De Franceschi, *Nat. Nanotechnol.* **9**, 79 (2014).
 [18] C. Janvier, L. Tosi, L. Bretheau, Ç. Ö. Girit, M. Stern, P. Bertet, P. Joyez, D. Vion, D. Esteve, M. F. Goffman, H. Pothier, and C. Urbina, *Science* **349**, 1199 (2015).
 [19] M. Hays, G. de Lange, K. Serniak, D. J. van Woerkom, D. Bouman, P. Krogstrup, J. Nygård, A. Geresdi, and M. H. Devoret, *Phys. Rev. Lett.* **121**, 047001 (2018).
 [20] M. Hays, V. Fatemi, D. Bouman, J. Cerrillo, S. Diamond, K. Serniak, T. Connolly, P. Krogstrup, J. Nygård, A. L. Yeyati, A. Geresdi, and M. H. Devoret, *Science* **373**, 430 (2021).
 [21] M. Pita-Vidal, A. Bargerbos, R. Žitko, L. J. Splitthoff, L. Grünhaupt, J. J. Westdorp, Y. Liu, L. P. Kouwenhoven, R. Aguado, B. van Heck, A. Kou, and C. K. Andersen, *ArXiv:2208.10094* (2022).

- [22] Z. Su, A. B. Tacla, M. Hocevar, D. Car, S. R. Plissard, E. P. A. M. Bakkers, A. J. Daley, D. Pekker, and S. M. Frolov, *Nat. Commun.* **8**, 1 (2017).
- [23] J.-D. Pillet, V. Benzoni, J. Griesmar, J.-L. Smir, and Ç. Ö. Girit, *Nano Lett.* **19**, 7138 (2019).
- [24] O. Kürtössy, Z. Scherübl, G. Fülöp, I. E. Lukács, T. Kanne, J. Nygård, P. Makk, and S. Csonka, *Nano Lett.* **21**, 7929 (2021).
- [25] K. Grove-Rasmussen, G. Steffensen, A. Jellinggaard, M. H. Madsen, R. Žitko, J. Paaske, and J. Nygård, *Nat. Commun.* **9**, 1 (2018).
- [26] J. C. Estrada Saldaña, A. Vekris, G. Steffensen, R. Žitko, P. Krogstrup, J. Paaske, K. Grove-Rasmussen, and J. Nygård, *Phys. Rev. Lett.* **121**, 257701 (2018).
- [27] D. Bouman, R. J. J. van Gulik, G. Steffensen, D. Pataki, P. Boross, P. Krogstrup, J. Nygård, J. Paaske, A. Pályi, and A. Geresdi, *Phys. Rev. B* **102**, 220505 (2020).
- [28] G. Wang, T. Dvir, G. P. Mazur, C.-X. Liu, N. van Loo, S. L. D. Ten Haaf, A. Bordin, S. Gazibegovic, G. Badawy, E. P. A. M. Bakkers, M. Wimmer, and L. P. Kouwenhoven, *Nature* **612**, 448 (2022).
- [29] T. Dvir, G. Wang, N. van Loo, C.-X. Liu, G. P. Mazur, A. Bordin, S. L. D. Ten Haaf, J.-Y. Wang, D. van Driel, F. Zatelli, X. Li, F. K. Malinowski, S. Gazibegovic, G. Badawy, E. P. A. M. Bakkers, M. Wimmer, and L. P. Kouwenhoven, *Nature* **614**, 445 (2023).
- [30] L. N. Bulaevskii, V. V. Kuzii, and A. A. Sobyanin, *JETP Lett. (USSR) (Engl. Transl.); (United States)* **25:7**, 314 (1977).
- [31] A. Martín-Rodero and A. Levy Yeyati, *Adv. Phys.* **60**, 899 (2011).
- [32] V. Meden, *J. Phys.: Condens. Matter* **31**, 163001 (2019).
- [33] A. V. Rozhkov and D. P. Arovas, *Phys. Rev. Lett.* **82**, 2788 (1999).
- [34] E. Vecino, A. Martín-Rodero, and A. L. Yeyati, *Phys. Rev. B* **68**, 035105 (2003).
- [35] A. Zazunov, V. S. Shumeiko, E. N. Bratus', J. Lantz, and G. Wendin, *Phys. Rev. Lett.* **90**, 087003 (2003).
- [36] S. Park and A. L. Yeyati, *Phys. Rev. B* **96**, 125416 (2017).
- [37] M. Leijnse and K. Flensberg, *Phys. Rev. B* **86**, 134528 (2012).
- [38] M. Žonda, V. Pokorný, V. Janiš, and T. Novotný, *Sci. Rep.* **5**, 1 (2015).
- [39] J. C. Cuevas, A. Levy Yeyati, and A. Martín-Rodero, *Phys. Rev. B* **63**, 094515 (2001).
- [40] M.-S. Choi, M. Lee, K. Kang, and W. Belzig, *Phys. Rev. B* **70**, 020502 (2004).
- [41] B. M. Andersen, K. Flensberg, V. Koerting, and J. Paaske, *Phys. Rev. Lett.* **107**, 256802 (2011).
- [42] M. Spethmann, X.-P. Zhang, J. Klinovaja, and D. Loss, *Phys. Rev. B* **106**, 115411 (2022).
- [43] J. Bauer, A. Oguri, and A. C. Hewson, *J. Phys.: Condens. Matter* **19**, 486211 (2007).
- [44] T. Meng, S. Florens, and P. Simon, *Phys. Rev. B* **79**, 224521 (2009).
- [45] J. Schindele, A. Baumgartner, R. Maurand, M. Weiss, and C. Schönenberger, *Phys. Rev. B* **89**, 045422 (2014).
- [46] A. Pöschl, A. Danilenko, D. Sabonis, K. Kristjūhan, T. Lindemann, C. Thomas, M. J. Manfra, and C. M. Marcus, *Phys. Rev. B* **106**, L241301 (2022).
- [47] T. Hayashi, T. Fujisawa, H. D. Cheong, Y. H. Jeong, and Y. Hirayama, *Phys. Rev. Lett.* **91**, 226804 (2003).
- [48] T. Fujisawa, T. Hayashi, H. D. Cheong, Y. H. Jeong, and Y. Hirayama, *Physica E* **21**, 1046 (2004).
- [49] G. Ithier, E. Collin, P. Joyez, P. J. Meeson, D. Vion, D. Esteve, F. Chiarello, A. Shnirman, Y. Makhlin, J. Schrieffer, and G. Schön, *Phys. Rev. B* **72**, 134519 (2005).
- [50] L. Glazman and G. Catelani, *SciPost Phys. Lect. Notes* , 031 (2021).
- [51] H. Paik, D. I. Schuster, L. S. Bishop, G. Kirchmair, G. Catelani, A. P. Sears, B. R. Johnson, M. J. Reagor, L. Frunzio, L. I. Glazman, S. M. Girvin, M. H. Devoret, and R. J. Schoelkopf, *Phys. Rev. Lett.* **107**, 240501 (2011).
- [52] D. Ristè, C. C. Bultink, M. J. Tiggelman, R. N. Schouten, K. W. Lehnert, and L. DiCarlo, *Nat. Commun.* **4**, 1 (2013).
- [53] X. Y. Jin, A. Kamal, A. P. Sears, T. Gudmundsen, D. Hover, J. Miloshi, R. Slattery, F. Yan, J. Yoder, T. P. Orlando, S. Gustavsson, and W. D. Oliver, *Phys. Rev. Lett.* **114**, 240501 (2015).
- [54] K. Serniak, M. Hays, G. de Lange, S. Diamond, S. Shankar, L. D. Burkhardt, L. Frunzio, M. Houzet, and M. H. Devoret, *Phys. Rev. Lett.* **121**, 157701 (2018).
- [55] A. P. Vepsäläinen, A. H. Karamlou, J. L. Orrell, A. S. Dogra, B. Loer, F. Vasconcelos, D. K. Kim, A. J. Melville, B. M. Niedzielski, J. L. Yoder, S. Gustavsson, J. A. Formaggio, B. A. VanDevender, and W. D. Oliver, *Nature* **584**, 551 (2020).
- [56] G. Kiršanskas, M. Goldstein, K. Flensberg, L. I. Glazman, and J. Paaske, *Phys. Rev. B* **92**, 235422 (2015).
- [57] D. G. Olivares, A. L. Yeyati, L. Bretheau, Ç. Ö. Girit, H. Pothier, and C. Urbina, *Phys. Rev. B* **89**, 104504 (2014).
- [58] A. Bargerbos, M. Pita-Vidal, R. Žitko, J. Ávila, L. J. Splitthoff, L. Grünhaupt, J. J. Wesdorp, C. K. Andersen, Y. Liu, L. P. Kouwenhoven, R. Aguado, A. Kou, and B. van Heck, *PRX Quantum* **3**, 030311 (2022).
- [59] J. J. Wesdorp, L. Grünhaupt, A. Vaartjes, M. Pita-Vidal, A. Bargerbos, L. J. Splitthoff, P. Krogstrup, B. van Heck, and G. de Lange, arXiv 10.48550/arXiv.2112.01936 (2021), 2112.01936.
- [60] R. J. Schoelkopf, P. Wahlgren, A. A. Kozhevnikov, P. Delsing, and D. E. Prober, *Science* **280**, 1238 (1998).
- [61] A. Aassime, G. Johansson, G. Wendin, R. J. Schoelkopf, and P. Delsing, *Phys. Rev. Lett.* **86**, 3376 (2001).
- [62] J. M. Elzerman, R. Hanson, J. S. Greidanus, L. H. Willems van Beveren, S. De Franceschi, L. M. K. Vandersypen, S. Tarucha, and L. P. Kouwenhoven, *Phys. Rev. B* **67**, 161308 (2003).
- [63] A. Blais, R.-S. Huang, A. Wallraff, S. M. Girvin, and R. J. Schoelkopf, *Phys. Rev. A* **69**, 062320 (2004).
- [64] P. Krantz, M. Kjaergaard, F. Yan, T. P. Orlando, S. Gustavsson, and W. D. Oliver, *Appl. Phys. Rev.* **6**, 021318 (2019).
- [65] F. Bloch and A. Siegert, *Phys. Rev.* **57**, 522 (1940).
- [66] We note that single-qubit gates in the strong tunneling regime could also be performed by detuning ε_ν . If the detuned quantum dot is capacitively coupled to a quantum dot from another qubit, a two-qubit rotation results only if the other quantum dot is also detuned (see Eq. (5)). To avoid accidental two-qubit gates when performing single-qubit operations, one can consider a design with divided tasks where only one quantum dot of each qubit is used for read-out and single-qubit gates by detuning ε_ν , while

the other quantum dot is capacitively coupled to other qubits.

- [67] I. H. Chan, R. M. Westervelt, K. D. Maranowski, and A. C. Gossard, *Appl. Phys. Lett.* **80**, 1818 (2002).
- [68] I. H. Chan, P. Fallahi, R. M. Westervelt, K. D. Maranowski, and A. C. Gossard, *Physica E* **17**, 584 (2003).
- [69] This equation is valid in the presence of an exact or approximate $U(1)$ spin-rotation symmetry around the axis of an applied Zeeman field or around the spin-orbit direction, such that perpendicular components can be treated perturbatively.
- [70] G. Burkard, T. D. Ladd, A. Pan, J. M. Nichol, and J. R. Petta, *Rev. Mod. Phys.* **95**, 025003 (2023).
- [71] A. M. J. Zwerver, T. Krähenmann, T. F. Watson, L. Lampert, H. C. George, R. Pillarisetty, S. A. Bojarski, P. Amin, S. V. Amitonov, J. M. Boter, R. Caudillo, D. Correas-Serrano, J. P. Dehollain, G. Droulers, E. M. Henry, R. Kotlyar, M. Lodari, F. Lüthi, D. J. Michalak, B. K. Mueller, S. Neyens, J. Roberts, N. Samkharadze, G. Zheng, O. K. Zietz, G. Scappucci, M. Veldhorst, L. M. K. Vandersypen, and J. S. Clarke, *Nat. Electron.* **5**, 184 (2022).
- [72] W. Gilbert, T. Tanttu, W. H. Lim, M. Feng, J. Y. Huang, J. D. Cifuentes, S. Serrano, P. Y. Mai, R. C. C. Leon, C. C. Escott, K. M. Itoh, N. V. Abrosimov, H.-J. Pohl, M. L. W. Thewalt, F. E. Hudson, A. Morello, A. Laucht, C. H. Yang, A. Saraiva, and A. S. Dzurak, *Nat. Nanotechnol.* **18**, 131 (2023).
- [73] G. Scappucci, C. Kloeffer, F. A. Zwanenburg, D. Loss, M. Myronov, J.-J. Zhang, S. De Franceschi, G. Katsaros, and M. Veldhorst, *Nature Reviews Materials* **6**, 926 (2021).
- [74] F. K. Malinowski, arXiv [10.48550/arXiv.2303.14410](https://arxiv.org/abs/10.48550/arXiv.2303.14410) (2023), [2303.14410](https://arxiv.org/abs/2303.14410).
- [75] G. O. Steffensen, private communication.
- [76] R. M. Lutchyn, E. P. A. M. Bakkers, L. P. Kouwenhoven, P. Krogstrup, C. M. Marcus, and Y. Oreg, *Nat. Rev. Mater.* **3**, 52 (2018).
- [77] E. Prada, P. San-Jose, M. W. A. de Moor, A. Geresdi, E. J. H. Lee, J. Klinovaja, D. Loss, J. Nygård, R. Aguado, and L. P. Kouwenhoven, *Nat. Rev. Phys.* **2**, 575 (2020).
- [78] K. Flensberg, F. von Oppen, and A. Stern, *Nature Reviews Materials* **6**, 944 (2021).
- [79] J. D. Sau and S. D. Sarma, *Nat. Commun.* **3**, 1 (2012).
- [80] W. Chang, S. M. Albrecht, T. S. Jespersen, F. Kuemmeth, P. Krogstrup, J. Nygård, and C. M. Marcus, *Nat. Nanotechnol.* **10**, 232 (2015).
- [81] P. Krogstrup, N. L. B. Ziino, W. Chang, S. M. Albrecht, M. H. Madsen, E. Johnson, J. Nygård, C. M. Marcus, and T. S. Jespersen, *Nat. Mater.* **14**, 400 (2015).
- [82] J. Shabani, M. Kjaergaard, H. J. Suominen, Y. Kim, F. Nichele, K. Pakrouski, T. Stankevic, R. M. Lutchyn, P. Krogstrup, R. Feidenhans'l, S. Kraemer, C. Nayak, M. Troyer, C. M. Marcus, and C. J. Palmstrøm, *Phys. Rev. B* **93**, 155402 (2016).
- [83] S. Vaitiekėnas, A. M. Whiticar, M.-T. Deng, F. Krizek, J. E. Sestoft, C. J. Palmstrøm, S. Marti-Sanchez, J. Arbiol, P. Krogstrup, L. Casparis, and C. M. Marcus, *Phys. Rev. Lett.* **121**, 147701 (2018).
- [84] Ö. Gül, H. Zhang, F. K. de Vries, J. van Veen, K. Zuo, V. Mourik, S. Conesa-Boj, M. P. Nowak, D. J. van Woerkom, M. Quintero-Pérez, M. C. Cassidy, A. Geresdi, S. Koelling, D. Car, S. R. Plissard, E. P. A. M. Bakkers, and L. P. Kouwenhoven, *Nano Lett.* **17**, 2690 (2017).
- [85] N. van Loo, G. P. Mazur, T. Dvir, G. Wang, R. C. Dekker, J.-Y. Wang, M. Lemang, C. Sfiligoj, A. Bordin, D. van Driel, G. Badawy, S. Gazibegovic, E. P. A. M. Bakkers, and L. P. Kouwenhoven, *Nat. Commun.* **14**, 1 (2023).
- [86] J. C. Estrada Saldaña, A. Vekris, R. Žitko, G. Steffensen, P. Krogstrup, J. Paaske, K. Grove-Rasmussen, and J. Nygård, *Phys. Rev. B* **102**, 195143 (2020).
- [87] A. W. Overhauser, *Phys. Rev.* **92**, 411 (1953).
- [88] Z. Wan, A. Kazakov, M. J. Manfra, L. N. Pfeiffer, K. W. West, and L. P. Rokhinson, *Nat. Commun.* **6**, 1 (2015).
- [89] M. Valentini, O. Sagi, L. Baghumyan, T. de Gijssels, J. Jung, S. Calcaterra, A. Ballabio, J. A. Servin, K. Aggarwal, M. Janik, T. Adlitzberger, R. S. Souto, M. Leijnse, J. Danon, C. Schrade, E. Bakkers, D. Chrastina, G. Isella, and G. Katsaros, arXiv [10.48550/arXiv.2306.07109](https://arxiv.org/abs/10.48550/arXiv.2306.07109) (2023), [2306.07109](https://arxiv.org/abs/2306.07109).
- [90] A. Tosato, V. Levajac, J.-Y. Wang, C. J. Boor, F. Borsoi, M. Botifoll, C. N. Borja, S. Martí-Sánchez, J. Arbiol, A. Sammak, M. Veldhorst, and G. Scappucci, *Commun. Mater.* **4**, 1 (2023).
- [91] M. Eich, R. Pisoni, A. Pally, H. Overweg, A. Kurzmann, Y. Lee, P. Rickhaus, K. Watanabe, T. Taniguchi, K. Ensslin, and T. Ihn, *Nano Lett.* **18**, 5042 (2018).
- [92] R. Garreis, C. Tong, J. Terle, M. J. Ruckriegel, J. D. Gerber, L. M. Gächter, K. Watanabe, T. Taniguchi, T. Ihn, K. Ensslin, and W. W. Huang, arXiv [10.48550/arXiv.2304.00980](https://arxiv.org/abs/10.48550/arXiv.2304.00980) (2023), [2304.00980](https://arxiv.org/abs/2304.00980).
- [93] H. Zhou, L. Holleis, Y. Saito, L. Cohen, W. Huynh, C. L. Patterson, F. Yang, T. Taniguchi, K. Watanabe, and A. F. Young, *Science* **375**, 774 (2022).
- [94] Y. Zhang, R. Polski, A. Thomson, É. Lantagne-Hurtubise, C. Lewandowski, H. Zhou, K. Watanabe, T. Taniguchi, J. Alicea, and S. Nadj-Perge, *Nature* **613**, 268 (2023).
- [95] G.-H. Lee, K.-F. Huang, D. K. Efetov, D. S. Wei, S. Hart, T. Taniguchi, K. Watanabe, A. Yacoby, and P. Kim, *Nat. Phys.* **13**, 693 (2017).
- [96] Ö. Gül, Y. Ronen, S. Y. Lee, H. Shapourian, J. Zauberman, Y. H. Lee, K. Watanabe, T. Taniguchi, A. Vishwanath, A. Yacoby, and P. Kim, *Phys. Rev. X* **12**, 021057 (2022).